Article

Laser spectroscopy and CP-violation sensitivity of actinium monofluoride

https://doi.org/10.1038/s41586-025-09814-1

Received: 7 July 2025

Accepted: 27 October 2025

M. Athanasakis-Kaklamanakis[1,2,3]✉, M. Au[4,5]✉, A. Kyuberis[6], C. Zülch[7], K. Gaul[7,8,9,10], H. Wibowo[11], L. Skripnikov[12], L. Lalanne[1,2], J. R. Reilly[4,13], Á. Koszorús[1,2], S. Bara[2], J. Ballof[5,9], R. Berger[1,7], C. Bernerd[4], A. Borschevsky[6], A. A. Breier[14,15], K. Chrysalidis[4], T. E. Cocolios[2], R. P. de Groote[2], A. Dorne[2], J. Dobaczewski[11], C. M. Fajardo Zambrano[2], K. T. Flanagan[13], S. Franchoo[16,17], J. D. Johnson[2], R. F. Garcia Ruiz[18,19], D. Hanstorp[20], S. Kujanpää[21], Y. C. Liu[22], K. M. Lynch[13], A. McGlone[13], N. S. Mosyagin[12], G. Neyens[2]✉, M. Nichols[20], L. Nies[1], F. Pastrana[18], S. Rothe[4], W. Ryssens[23,24], B. van den Borne[2], J. Wessolek[4,13], S. G. Wilkins[18,19] & X. F. Yang[22]

The apparent invariance of the strong nuclear force under combined charge conjugation and parity (CP) remains an open question in modern physics[1,2]. Precision experiments with heavy atoms and molecules can provide stringent constraints on CP violation via searches for effects due to permanent electric dipole moments and other CP-odd properties in leptons, hadrons and nuclei[3]. Radioactive molecules have been proposed as highly sensitive probes for such searches[4], but experiments with most such molecules have so far been beyond technical reach. Here we report the production and spectroscopic study of a gas-phase actinium molecule, ^{227}AcF. We observe the predicted strongest electronic transition from the ground state, which is necessary for efficient readout in searches of symmetry-violating interactions. Furthermore, we perform electronic- and nuclear-structure calculations for ^{227}AcF to determine its sensitivity to various CP-violating parameters, and find that a realistic, near-term experiment with a precision of 1 mHz would improve current constraints on the CP-violating parameter hyperspace by 3 orders of magnitude. Our results thus highlight the potential of ^{227}AcF for exceptionally sensitive searches of CP violation.

Providing a satisfactory explanation for the cosmological baryon asymmetry requires that the combined symmetry of charge conjugation and parity (CP) is broken, following Sakharov's conditions[5]. Within the Standard Model of particle physics, CP violation emerges in the weak nuclear force via the complex phase of the Cabibbo–Kobayashi–Maskawa matrix, which is responsible for the observed CP-violating decay of K mesons, and in the strong nuclear force via a term quantified by the quantum chromodynamics (QCD) $\bar{\theta}$ phase. The upper bounds to CP-violating terms within the Standard Model are considered not to be able to account for the observed baryon asymmetry in the Universe[2], and thus new sources of CP violation are theorized to exist. Signatures of leptonic, hadronic and nuclear CP-odd properties manifest as symmetry-violating electromagnetic moments, which in turn lead to transition frequency shifts in atoms and molecules that can in principle be observed via high-precision measurements. These systems thus offer a sensitive approach to search for CP violation and physics beyond the Standard Model[3].

Owing to the electrostatic screening by the bound electrons, neutral atoms and molecules are not suitable probes for measurements of the CP-odd electric dipole moment (EDM) of the nucleus[6]. Instead, experiments search for the closely related nuclear Schiff moment[7], which is linked to the QCD Lagrangian via a chiral effective field theory of the pion–nucleon interaction[8–10]. Despite global experimental efforts to measure the Schiff moment in ^{199}Hg (ref. 11), ^{205}Tl (ref. 12), ^{225}Ra (ref. 13) and other nuclei, only upper bounds have been determined so far. Future efforts to improve experimental precision are thus accompanied by theoretical investigations to identify nuclei with an enhanced Schiff moment, thus maximizing the chances of observing a non-zero signal in the laboratory.

Heavy radioactive nuclei with static octupole deformation have enhanced Schiff moments in their intrinsic (body-fixed) frame of reference, owing to the close-lying opposite-parity states of same angular momentum that arise from their reflection-asymmetric shape[10,14]. Of the nuclei that have been theoretically investigated so far, the longest-lived

---

[1] Experimental Physics Department, CERN, Geneva, Switzerland. [2] Instituut voor Kern- en Stralingsfysica, KU Leuven, Leuven, Belgium. [3] Centre for Cold Matter, Imperial College London, London, UK. [4] Systems Department, CERN, Geneva, Switzerland. [5] Department of Chemistry, Johannes Gutenberg-Universität Mainz, Mainz, Germany. [6] Van Swinderen Institute of Particle Physics and Gravity, University of Groningen, Groningen, Netherlands. [7] Fachbereich Chemie, Philipps-Universität Marburg, Marburg, Germany. [8] Helmholtz Institute Mainz, Mainz, Germany. [9] GSI Helmholtzzentrum für Schwerionenforschung GmbH, GSI, Darmstadt, Germany. [10] Institut für Physik, Johannes Gutenberg-Universität Mainz, Mainz, Germany. [11] School of Physics, Engineering and Technology, University of York, York, UK. [12] Affiliation covered by a cooperation agreement with CERN at the time of the experiment, Geneva, Switzerland. [13] Department of Physics and Astronomy, The University of Manchester, Manchester, UK. [14] Institut für Physik und Astronomie, Technische Universität Berlin, Berlin, Germany. [15] Laboratory for Astrophysics, Institute of Physics, University of Kassel, Kassel, Germany. [16] Laboratoire Irène Joliot-Curie, Orsay, France. [17] University Paris-Saclay, Orsay, France. [18] Department of Physics, Massachusetts Institute of Technology, Cambridge, MA, USA. [19] Laboratory for Nuclear Science, Massachusetts Institute of Technology, Cambridge, MA, USA. [20] Department of Physics, University of Gothenburg, Gothenburg, Sweden. [21] Department of Physics, University of Jyväskylä, Jyväskylä, Finland. [22] School of Physics and State Key Laboratory of Nuclear Physics and Technology, Peking University, Beijing, China. [23] Institut d'Astronomie et d'Astrophysique, Université libre de Bruxelles, Brussels, Belgium. [24] Brussels Laboratory of the Universe - BLU-ULB, Université libre de Bruxelles, Brussels, Belgium.
✉e-mail: m.athkak@cern.ch; mia.au@cern.ch; gerda.neyens@kuleuven.be

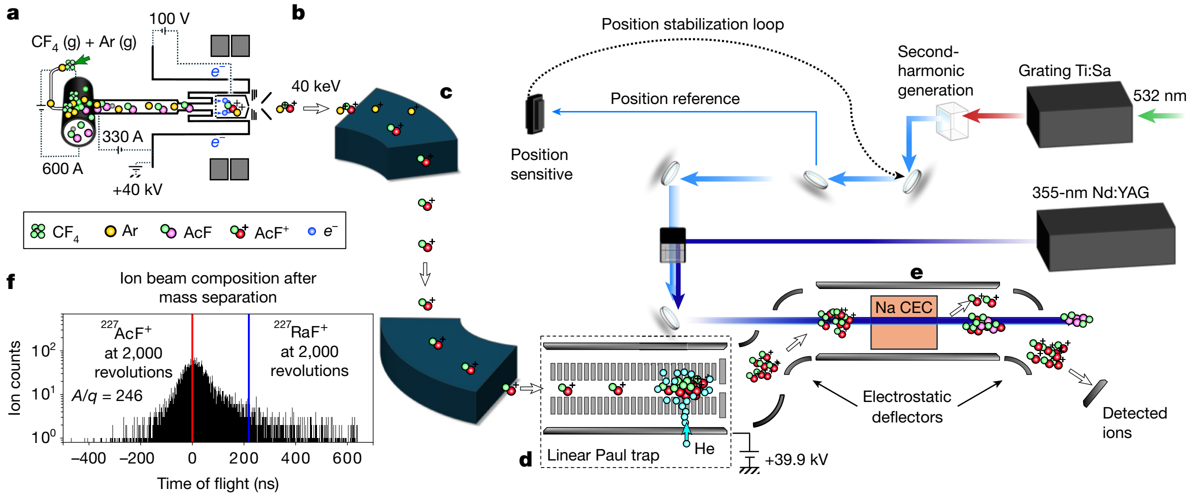

Fig. 1 | Schematic of the experiment. **a**, Target and ion-source unit releasing Ac to form AcF_x molecules from injected CF_4. **b**, All species are ionized by accelerated electrons within the anode volume and extracted across a voltage difference (40 kV) to ground potential. **c**–**f**, The ion beam is then mass-separated (**c**), cooled and bunched (**d**) before neutralization via charge exchange with sodium vapour in the charge-exchange cell (CEC), and laser resonance ionization (**e**). **f**, The time-of-flight spectrum of the ion beam with mass-to-charge ratio $A/q = 246$ after 2,000 revolutions in a multi-reflection time-of-flight mass spectrometer[23,49]. The expected times of flight for $^{227}Ac^{19}F^+$ (half-life $t_{1/2} = 21.8$ yr) and $^{227}Ra^{19}F^+$ ($t_{1/2} = 42.5$ min) are shown in red and blue lines, respectively. The x axis is offset by the expected time of flight for $^{227}Ac^{19}F^+$. No molecules other than $^{227}Ac^{19}F^+$ were identified in the beam.

actinium isotopes ^{225,227}Ac are expected to have the largest nuclear Schiff moments[14], and Mössbauer spectroscopy of ^{227}Ac has recently been proposed as a possible pathway to study its CP-violating odd-electric and even-magnetic nuclear moments[15]. Experiments with heavy polar molecules are currently the most sensitive approach to search for hadronic, leptonic and nuclear CP-violating properties[3], owing to their enormous internal electric field and high polarizability in the presence of small applied fields. Therefore, precision experiments using polar actinium molecules, such as actinium monofluoride (AcF), offer the most compelling direction for searches of CP violation with heavy and deformed actinium nuclei.

The longest-lived actinium isotope ^{227}Ac has a half-life of 21.8 years and a long decay chain of radioactive products. Thus, manufacturing macroscopic actinium samples and transporting them for use with existing experimental set-ups for EDM searches would be prohibitively radioactive. Radioactive ion beam facilities such as CERN-ISOLDE[16] are able to deliver actinium molecules for study, offering the ability to perform experiments with such compounds in environments with appropriate radiation-protection measures in place. So far, molecular formation of radioactive species produced via the isotope separation on line (ISOL) method[17,18] used at the CERN-ISOLDE facility has been proven to reliably deliver isotopically pure ion beams of radioactive molecules. Controlled formation of molecules within the ISOL source environment is additionally used for purification of radioactive ion beams from contaminants, and for improving the extraction efficiency of the radioactive isotopes[17,19,20]. Past investigations using the ISOL method demonstrate that in addition to exhibiting limited extraction efficiency owing to its refractory chemical properties[21], actinium also forms highly refractory ceramics in an oxygen-rich environment[22]. This limits extraction rates of actinium itself as well as its oxides and nitrides, motivating developments to form and extract the more volatile fluoride ions to reach higher extraction rates[23]. As the shot-noise-limited precision scales with the square root of the number of probed molecules[24], the availability of AcF contributes significantly to its potential as a compelling system for precision spectroscopy.

Production and spectroscopy of AcF

No experimental spectroscopic study of AcF has been reported so far. Detailed knowledge of the strongest electronic transition from the $X^1\Sigma^+$ ground state is critical, as the $X^1\Sigma^+$ state is envisioned for precision measurements and is not limited by a finite radiative lifetime like the metastable $^3\Delta_1$ electronic states in ThO and HfF^+ that have been used in electron EDM studies. Knowledge of the strongest transition from $X^1\Sigma^+$ is necessary to assess the state readout efficiency via optical detection and the potential for laser cooling. State-readout efficiency is in turn crucial for a sensitive high-precision experiment[12,24,25]. Therefore, spectroscopic experiments are required to characterize the relevant properties of AcF, while also providing a versatile benchmark of predictive relativistic ab initio quantum chemistry for radioactive molecules[4,26], as recently applied on AcF[27].

In this work, intense, chemically and isotopically pure beams of $^{227}Ac^{19}F^+$ were produced at the CERN-ISOLDE facility, as shown in Fig. 1. Actinium nuclides were produced in nuclear reactions induced by 1.4-GeV protons from the CERN Proton Synchrotron Booster bombarding a thick, room-temperature target of uranium carbide (UC_x). Two weeks after proton irradiation, the radiogenic actinium nuclides were extracted by resistively heating the target to >1,300 °C, facilitating nuclide diffusion and effusion through the UC_x matrix[28]. Carbon tetrafluoride (CF_4) was supplied to the heated target at a rate of 0.065 nmol s^{-1} for the formation of fluoride molecules (Fig. 1a). Ionization techniques using hot cavities and resonance laser ionization are most frequently used at ISOLDE, but without further information on its chemical properties, these techniques could not be used to produce AcF. A forced-electron-beam-induced arc-discharge ion source[29] was connected to the target to create ions of the extracted species through electron impact, plasma ionization and molecular dissociation (Fig. 1b).

The ion beam was accelerated to 40 keV and the $^{227}Ac^{19}F^+$ ions were separated from all other radiogenic products using two magnetic dipole separators in series (Fig. 1c). The temperature of the target was controlled to regulate the mass-separated $^{227}Ac^{19}F^+$ ion beam at an intensity between 6×10^6 and 2×10^7 ions per second for the duration of the experiment. Although an intensity of more than 6×10^7 ions per second could be achieved at higher temperature, the higher rates correspondingly deplete the in-target actinium inventory faster. The continuous, isotopically purified beam of $^{227}Ac^{19}F^+$ was then accumulated in a linear Paul trap that reduced the internal temperature of the molecules via collisions with room-temperature helium and released the cooled ion beam in 5-μs bunches every 10 ms (Fig. 1d).

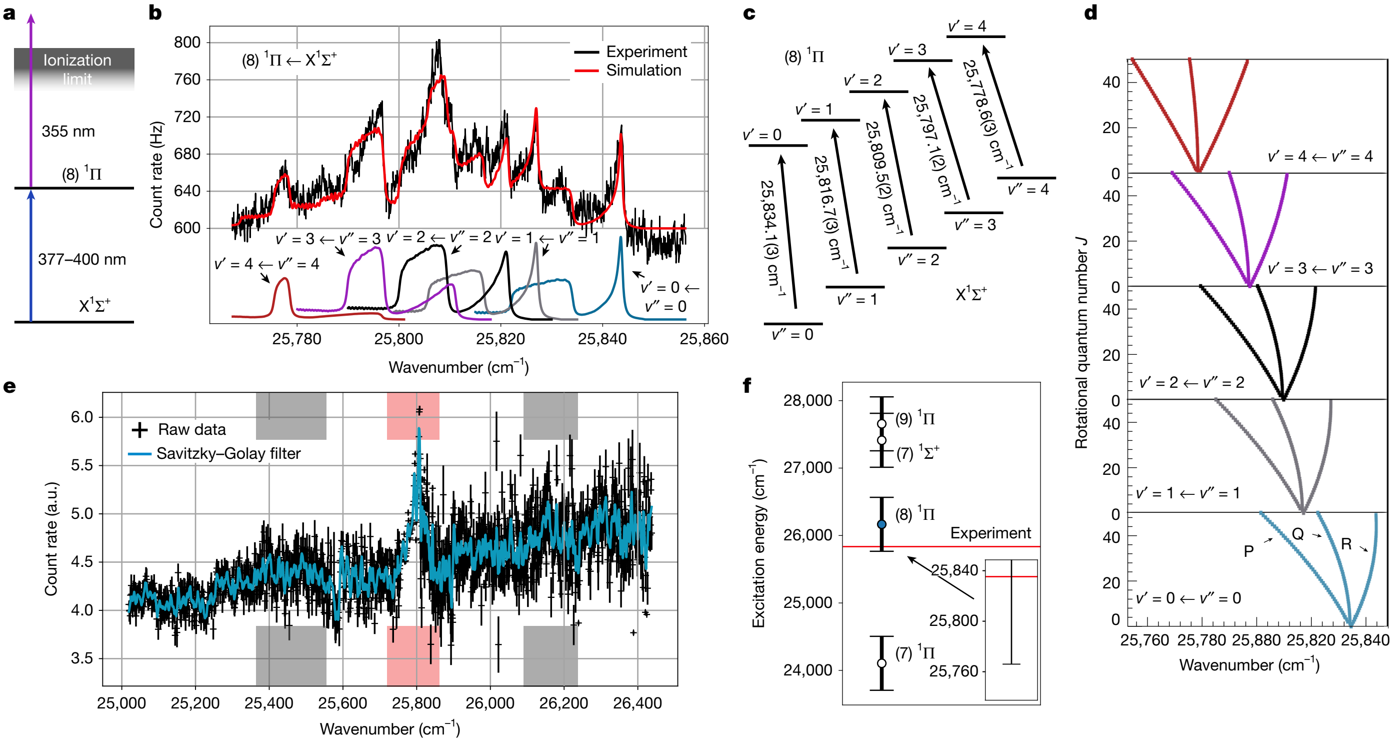

Fig. 2 | Spectroscopy of AcF. a, Two-step laser resonance ionization scheme used to search for electronic transitions in AcF. **b**, Spectrum of the measured vibronic transitions from the ground state in AcF, and simulation based on the contour-fitted molecular constants. **c**, Assigned vibronic transitions observed in the spectrum shown in **b**. **d**, Fortrat diagrams for the measured vibronic transitions, showing the evolution of the P, Q and R branches along the diagonal vibrational progression. **e**, Ion count rate as a function of the wavenumber of the first excitation laser across the full scanning range. A cubic Savitzky–Golay de-noising filter with a ten-point window length is applied to the raw data to assist in the visualization of data trends. The complete spectrum is constructed from multiple shorter scans. A vertical offset is applied to each scan to compensate for their different background rates owing to long-term variations in the beam intensity. The *y* axis is thus in arbitrary units. The red band marks the region of the spectrum in **b** and the grey bands mark regions investigated and excluded as resonant features. **f**, Comparison of excitation wavenumbers with different electronic states calculated with FS-RCC[27] and the upper state in the spectrum of **b**. The error bars correspond to the theoretical uncertainty in the excitation wavenumber calculations, as reported in ref. 27.

The bunched ion beam was delivered to the collinear resonance ionization spectroscopy (CRIS) experiment[30] (Fig. 1e). Following in-flight neutralization in a charge-exchange cell of sodium vapour (about 210 °C), the ions that were not neutralized were discarded by electrostatically deflecting them away from the neutral beam. Spectroscopy of ^{227}AcF was performed at CRIS to search for electronic transitions from the ground state using a two-step pulsed laser scheme (Fig. 2a). Ultraviolet light was produced by single-pass second-harmonic generation (SHG) of a pulsed titanium:sapphire (Ti:Sa) laser and was scanned between 377 nm and 400 nm to search for a resonant transition from the $X^1\Sigma^+$ ground state of AcF. A high-power third-harmonic pulsed neodymium-doped yttrium aluminium garnet (Nd:YAG) laser at 355 nm followed as the second step to non-resonantly ionize the molecules found in an excited electronic state when the first laser step was at the resonant frequency of an electronic transition from $X^1\Sigma^+$. To continuously scan a broad wavenumber range (approximately 1,400 cm^{-1}) with the second-harmonic Ti:Sa light, a position-stabilization loop was implemented along with stabilization of the SHG crystal angle to optimize the SHG output power. Further information on the production and spectroscopy can be found in Methods.

Extensive relativistic Fock-space coupled cluster calculations (FS-RCC)[27] predict only one transition from $X^1\Sigma^+$ to an excited electronic state in the scanned wavenumber range, and its calculated transition dipole moment is the largest among all transitions from $X^1\Sigma^+$. The only resonance across the full scan range (Fig. 2e) was observed from 25,770 cm^{-1} to 25,860 cm^{-1}, shown in Fig. 2b. On the basis of the FS-RCC calculations, this spectrum corresponds to the diagonal vibrational progression of $(8)^1\Pi \leftarrow X^1\Sigma^+$, calculated to be the strongest transition from the ground state, and thus the optimal choice for a high-efficiency optical state-readout scheme in a future precision experiment. With the assistance of calculated molecular constants and Franck–Condon factors (FCFs) for AcF$^+$ and AcF, the peaks in the spectrum were assigned as shown in Fig. 2c,d (see Methods for details). The calculated FCFs for allowed electronic transitions to other electronic states in the vicinity of $(8)^1\Pi$ are highly diagonal[27]. Therefore, it appears unlikely that the observed spectrum belongs to an overtone and non-diagonal vibrational progression from $X^1\Sigma^+$ to a state other than $(8)^1\Pi$, whereas the diagonal vibrational progression to $(8)^1\Pi$ is not observed. Other wavenumber regions were further investigated, shown as grey bands in Fig. 2e around 25,400 cm^{-1} and 26,150 cm^{-1}. In these regions, the number of resonantly ionized molecules was not affected by the presence or absence of the scanning laser in the interaction region. These regions were thus excluded as transitions corresponding to a resonant excitation from the ground state. The measured excitation energy for the upper state in the spectrum in Fig. 2b is in agreement with the ab initio calculations for the $(8)^1\Pi$ state[27], as shown in Fig. 2f.

The contour of the different $v' \leftarrow v''$, $v' = v''$ (where v'' is the vibrational quantum number of the lower state and v' of the upper) transitions of the measured vibrational progression visibly changes shape as v'' increases (Fig. 2b). This is the result of a gradual change in the slope of the P, Q and R rotational branches for increasing v'', as shown in Fig. 2d. In addition, the observed spacing between vibrational transitions becomes uneven for $v'' > 1$ (Fig. 2b,c). At the present time, the origin of this is unclear. Rotationally resolved spectroscopy in the future is necessary to provide additional information regarding the anharmonicity of the vibrational potential in the electronic states involved.

The radiative lifetime of the $(8)^1\Pi$ state was calculated to be τ_{calc} = 6.65 ns (ref. 27). The lifetime of the observed upper electronic state was

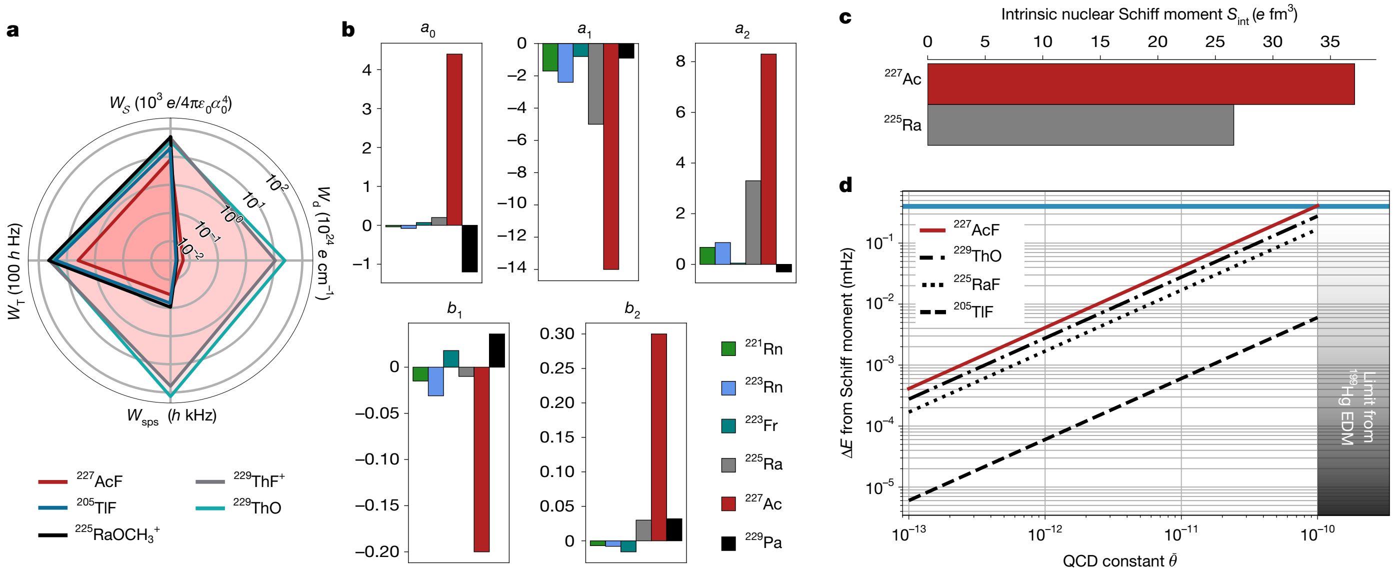

Fig. 3 | Molecular and nuclear sensitivity to CP violation. **a**, Comparison of molecular sensitivity to the nuclear Schiff moment (W_S), tensor-pseudotensor electron–nucleon interaction (W_T), EDM of the electron (W_d) and scalar-pseudoscalar electron–nucleon interaction (W_{sps}) for the $^3\Delta_1$ electronic states in ^{229}ThO and ^{229}ThF$^+$, and for the $^1\Sigma^+$ electronic ground states in ^{227}AcF, ^{205}TlF and ^{225}RaOCH$_3$$^+$. **b**, Comparison of the sensitivity coefficients (in units of e fm^3) of the laboratory nuclear Schiff moment to the CP-odd pion–nucleon (isoscalar a_0, isovector a_1, isotensor a_2) and heavy-meson-exchange (b_1, b_2) interactions for different nuclei. Values for ^{227}Ac are from this work and for all other nuclei from ref. 10. **c**, Comparison of the nuclear Schiff moment in the intrinsic body-fixed frame (S_{int}) for ^{227}Ac and ^{225}Ra, calculated with NDFT in this work and in ref. 10. **d**, Expected magnitude of the CP-odd molecular energy shift in the laboratory due to the Schiff moment as a function of the QCD constant $\bar{\theta}$ for different molecules, taking into account the calculated W_S constant for each species. The teal line marks the precision needed to place a new bound on $\bar{\theta}$ using ^{227}AcF.

investigated experimentally, but only an upper limit (equal to the pulse width of the excitation laser) could be determined at $\tau_{exp} \leq 38(4)$ ns, via the experimental approach previously applied to RaF[31]. Consequently, a lower limit on the radiative decay rate is set at $\Gamma \geq 2.6(3) \times 10^7$ s^{-1}. The strength of the measured transition corroborates the assignment of the upper state as (8)$^1\Pi$. Future experimental study is of interest to provide a direct lifetime measurement.

To assess the potential of a precision experiment with ^{227}AcF to constrain CP violation, electronic- and nuclear-structure calculations of the molecular sensitivity to CP-odd properties are necessary. The sensitivity W_S of the X$^1\Sigma^+$ state to the nuclear Schiff moment was calculated in refs. 32,33, where the prominent role of electron correlation in the magnitude of W_S was highlighted. Owing to cancellation effects of the individual molecular orbital contributions, the impact of electron correlation on W_S was found to be more pronounced (>20%) in AcF than in other actinium molecules. Relativistic coupled cluster calculations using the full four-component Dirac–Coulomb and Dirac–Coulomb–Gaunt Hamiltonians were thus performed in this work for dedicated investigations of W_S in AcF, using current state-of-the-art quantum chemistry techniques at a high degree of accuracy. The obtained final value of $W_S = -7{,}748(545)\, e/4\pi\epsilon_0 a_0^4$ (where ϵ_0 is the vacuum permittivity and a_0 is the Bohr radius) for the X$^1\Sigma^+$ state incorporates higher-order effects than the results reported in the previous studies[32,33], and provides a transparent and robust uncertainty analysis. A detailed uncertainty breakdown is given in Methods and comparison with past studies in Supplementary Information.

Impact on the CP-violation hyperspace

The nuclear Schiff moment is not the only source of the molecular CP-odd signal that experiments would seek to measure in the laboratory. Other leptonic, hadronic and nuclear CP-odd properties, such as the electron EDM, would similarly give rise to a molecular EDM, and must be accounted for by calculating the sensitivity of the molecule to the different sources of CP violation. Utilizing the toolbox approach described in ref. 34, the sensitivity of the X$^1\Sigma^+$ ground state of AcF to the CP-odd nuclear Schiff moment (W_S), tensor-pseudotensor electron–nucleon interaction (W_T), electron EDM (W_d) and scalar-pseudoscalar electron–nucleon interaction (W_{sps}) were calculated in this work within the two-component zeroth-order regular-approximation complex generalized Hartree–Fock (2c-ZORA-cGHF) framework. The factors are compared with those of other molecules in Fig. 3a. In closed-shell molecules such as AcF and RaOCH$_3$$^+$ ($^1\Sigma^+$), W_d and W_{sps} are strongly suppressed by the electron-to-proton mass ratio compared with open-shell molecules such as HfF$^+$ and ThO ($^3\Delta_1$). Sensitivity to these interactions can only emerge owing to electron magnetization by the nuclear magnetic dipole moment, giving rise to the second-order properties W_d^m and W_{sps}^m. For ^{227}AcF, they are calculated to be $W_d^m = -5 \times 10^{-4}$ GV (cmμ_N)$^{-1}$ and $W_{sps}^m = -2 \times 10^{-3}$ peV μ_N^{-1}, where μ_N is the nuclear magneton. Closed- and open-shell molecules thus provide complementary information on sources of CP violation[35–37], and experiments using different molecules are necessary.

To estimate the impact of an experiment using ^{227}AcF within the global landscape of CP-odd searches with atoms and molecules, the value of W_S has to be combined with nuclear-structure calculations of the Schiff moment of the ^{227}Ac nucleus. Previous theoretical investigations of the nuclear Schiff moment in the intrinsic, body-fixed frame (S_{int}) of ^{227}Ac relied on nuclear density functional theory (NDFT) calculations of S_{int} in the neighbouring ^{225}Ra (ref. 38), and semi-empirical scaling factors based on the intrinsic quadrupole and octupole deformation and parity spacing of ^{225}Ra and ^{227}Ac (ref. 14). This estimation indicated that ^{227}Ac has the largest laboratory-frame Schiff moment S_{lab} across all investigated nuclei. To confirm this result within a rigorous theoretical framework, a direct NDFT calculation of both S_{int} and S_{lab} in ^{227}Ac was performed in this work. The calculated value $S_{int}(^{227}\text{Ac}) = 37.1(16)\, e$ fm^3 is 40% higher than $S_{int}(^{225}\text{Ra}) = 26.6(19)\, e$ fm^3 (ref. 10; Fig. 3c).

For a nucleus with a low-lying state $\overline{\Psi}_0$ with the same angular momentum but opposite parity as the ground state Ψ_0, the laboratory-frame nuclear Schiff moment S_{lab} can be approximated as[10]

Table 1 | Sensitivity coefficients (in units of e fm^3) of the laboratory Schiff moment of ^{227}Ac to the isoscalar (a_0), isovector (a_1) and isotensor (a_2) CP-odd pion–nucleon coupling constants and CP-odd heavy-meson-exchange coupling constants (b_1, b_2), calculated with NDFT in this work

	a_0	a_1	a_2	b_1	b_2
^{227}Ac	4.4(10)	−14.0(18)	8.3(31)	−0.2(2)	0.3(3)

$$S_{\mathrm{lab}} \approx -2\ \mathrm{Re}\left\{\frac{\langle \Psi_0|\hat{S}|\overline{\Psi}_0\rangle\langle \overline{\Psi}_0|\hat{V}_{\mathrm{P,T}}|\Psi_0\rangle}{E_{\overline{\Psi}_0} - E_{\Psi_0}}\right\}, \tag{1}$$

where $\hat{S}$ is the Schiff operator, $E_{\overline{\Psi}_0}$ is the energy of state $\overline{\Psi}_0$ and $\hat{V}_{\mathrm{P,T}}$ is the CP-violating nuclear potential that precision experiments aim to elucidate. S_{lab} can also be expressed parametrically in terms of the CP-odd coupling constants within $\hat{V}_{\mathrm{P,T}}$ as

$$S_{\mathrm{lab}} = a_0 g\overline{g}_0 + a_1 g\overline{g}_1 + a_2 g\overline{g}_2 + b_1\overline{c}_1 + b_2\overline{c}_2, \tag{2}$$

where g is the QCD pion–nucleon coupling constant, $\overline{g}_i$ are unknown isoscalar, isovector and isotensor CP-odd pion–nucleon coupling constants, $\overline{c}_i$ are unknown CP-odd zero-range heavy-meson-exchange coupling constants, and a_i, b_i are sensitivity coefficients. The constants $\overline{g}_i$ and $\overline{c}_i$ are sought to be extracted from precision experiments, whereas the sensitivity coefficients a_i, b_i need to be determined from nuclear-structure calculations.

In ^{227}Ac, the energy difference $E_{\overline{\Psi}_0} - E_{\Psi_0}$ between the $I^{\pi} = \frac{3}{2}^-$ ground state Ψ_0 and the lowest-lying $I^{\pi} = \frac{3}{2}^+$ partner state $\overline{\Psi}_0$ is only 27.369 keV (ref. 39). Table 1 shows the S_{lab} sensitivity coefficients in ^{227}Ac as determined from the NDFT calculation, and Fig. 3b compares the sensitivity coefficients in ^{227}Ac with those in ^{221,223}Rn, ^{223}Fr, ^{225}Ra and ^{229}Pa (ref. 10). Evidently, the Schiff moment in ^{227}Ac is significantly more sensitive to all CP-odd interactions than the other nuclei, including ^{225}Ra, which is currently under experimental investigation using ultracold atoms[13]. Inversely, for a given magnitude of $\overline{g}_i$ and $\overline{c}_i$, the laboratory Schiff moment of ^{227}Ac will be larger than for the other nuclides, which makes actinium molecules that are sensitive to $S_{\mathrm{lab}}(^{227}\mathrm{Ac})$ highly promising probes for the first measurement of a nuclear CP-odd property.

The S_{lab} moment can also be expressed in terms of the QCD $\overline{\theta}$ phase, based on the relationships $g\overline{g}_0 = 0.21\overline{\theta}$ and $g\overline{g}_1 = -0.046\overline{\theta}$ (refs. 14,40–42). Combined with the nuclear sensitivity coefficients a_0, a_1 and the molecular sensitivity to the Schiff moment $W_{\mathcal{S}}$, the expected molecular energy shift in the laboratory owing to the nuclear Schiff moment can be estimated as a function of $\overline{\theta}$. Figure 3d compares the expected energy shift in ^{227}AcF, ^{229}ThO, ^{225}RaF and ^{205}TlF. Evidently, although $W_{\mathcal{S}}$ is of moderate magnitude in AcF compared with other molecules (Fig. 3a), a precision experiment using ^{227}AcF would have the highest sensitivity to $\overline{\theta}$ across the considered species. Specifically, an experiment using ^{227}AcF with an uncertainty of 0.1 mHz, as achieved in 1989 using ^{205}TlF (ref. 43), would place a more stringent limit on $\overline{\theta}$, which is currently set at $\overline{\theta} < 1.5 \times 10^{-10}$ via the ^{199}Hg EDM[11]. It must be noted that as no calculations have been reported on the relationship between $\overline{\theta}$ and $g\overline{g}_2$, and $\overline{c}_1$ and $\overline{c}_2$, their contribution to the results shown in Fig. 3d are set to zero.

The computed S_{lab} sensitivity coefficients a_0, a_1 for ^{227}Ac can be combined with a rough order-of-magnitude estimate for the volume interaction R_{vol} with the short-range contribution to the proton EDM as $R_{\mathrm{vol}} \approx \frac{3(1.2\ \mathrm{fm})^2 A^{2/3}}{50}$ (where A is the mass number) following ref. 44, and the electronic-structure calculations of $W_{\mathcal{S}}$, W_{m}, W_{T}, W_{p}, W_{d} and W_{sps} for AcF. The expected impact that an experiment with ^{227}AcF would have on the constraints of different CP-violating parameters can then be extracted from a global analysis[35,36] that incorporates previously reported EDM experiments using ^{129}Xe, ^{171}Yb, ^{133}Cs, ^{199}Hg, ^{205}Tl, ^{225}Ra, ^{174}YbF, ^{180}HfF$^+$, ^{205}TlF, ^{207}PbO and ^{232}ThO. A global analysis of CP violation was performed in this work as per ref. 36, assuming two separate experiments with ^{227}AcF with respective precision of 1 mHz and 0.1 mHz.

The unconstrained level of CP violation is expressed as a region enclosed by experimental limits within a multi-dimensional hyperspace, whose dimensions correspond to the experimentally measurable CP-odd properties. Here, a seven-dimensional hyperspace is considered, formed by the tensor-pseudoscalar k_{T}, scalar-pseudoscalar k_{sps} and pseudoscalar-scalar k_{p} nucleon–electron current interaction coupling constants, the electron EDM d_{e}, the short-range nucleon EDM $d_{\mathrm{p}}^{\mathrm{sr}}$, and the isoscalar $\overline{g}_0$ and isovector $\overline{g}_1$ pion–nucleon interaction coupling constants. This results in the following effective Hamiltonian for each atom and molecule in the global analysis, including ^{227}AcF

$$\begin{aligned} H^{P,T} = {} & \Omega[W_{\mathrm{d}}d_{\mathrm{e}} + W_{\mathrm{sps}}k_{\mathrm{sps}}] \\ & + \Theta W_{\mathcal{M}}[\mathcal{M}_{\mathrm{EDM}}d_{\mathrm{p}}^{\mathrm{sr}} + g a_{\mathcal{M},0}\overline{g}_0 + g a_{\mathcal{M},1}\overline{g}_1] \\ & + \mathcal{I}[W_{\mathrm{T}}k_{\mathrm{T}} + W_{\mathrm{p}}k_{\mathrm{p}} + W_{\mathrm{sps}}^{\mathrm{m}}\gamma k_{\mathrm{sps}} + W_{\mathcal{S}}(g a_0\overline{g}_0 + g a_1\overline{g}_1) \\ & + W_{\mathrm{d}}^{\mathrm{m}}\gamma d_{\mathrm{e}} + W_{\mathrm{m}}\eta_{\mathrm{p}}d_{\mathrm{p}}^{\mathrm{sr}} + W_{\mathcal{S}}R_{\mathrm{vol}}d_{\mathrm{p}}^{\mathrm{sr}}], \end{aligned} \tag{3}$$

where Ω and $\mathcal{I}$ are the projections of the total electronic $\mathbf{J}_{\mathrm{e}}$ and nuclear angular momentum $\mathbf{I}$ on the molecular axis, Θ is the projection of the product of $\mathbf{J}_{\mathrm{e}}$ with the second-order tensor of $\mathcal{I}$ on the molecular axis, $W_{\mathcal{M}}$ is the electronic-structure constant for the interaction with a nuclear magnetic quadrupole moment (NMQM), $\mathcal{M}_{\mathrm{EDM}}$ and $a_{\mathcal{M},0}$ and $a_{\mathcal{M},1}$ are nuclear-structure constants for different contributions to the NMQM, $\eta_{\mathrm{p}} = \frac{\mu_{\mathrm{N}}}{A} + \frac{\mu}{Z}$ with Z being the atomic number and μ the nuclear magnetic dipole moment, and γ is the nuclear gyromagnetic ratio $\gamma = \mu/I$. For ^{227}AcF, $\Omega = \Theta = 0$, $\eta_{\mathrm{p}} = 0.01811\,\mu_{\mathrm{N}}$ and $\gamma = 0.8133\,\mu_{\mathrm{N}}$. The CP-violation parameters, electronic-structure coefficients W_i and nuclear-structure coefficients are defined as in ref. 36.

In Fig. 4, selected two-dimensional subspaces of the seven-dimensional hyperspace are presented, in which ^{227}AcF would have a determining role, for the two assumed values of ^{227}AcF precision δf at 1 mHz and 0.1 mHz. Plots of all two-dimensional subspaces are provided in Supplementary Information. It is found that a precision experiment with ^{227}AcF would reduce the volume of the seven-dimensional coverage region by a factor of 6×10^3 for $\delta f = 1$ mHz, and by 6×10^4 for $\delta f = 0.1$ mHz. This can be understood as a result of the complementarity between an experiment with ^{227}AcF and existing results using other closed-shell systems, such as ^{199}Hg, which can be seen in Fig. 4, and the high sensitivity of the ^{227}Ac nucleus to CP violation.

The precision assumed for the ^{227}AcF experiment in the global analysis can be realistically achieved with the demonstrated production rates of ^{227}AcF at CERN-ISOLDE in this work and conservative estimates for a precision set-up. The statistical uncertainty of a spin-precession frequency measurement using Ramsey interferometry at the shot-noise limit is[12]

$$\delta f = \frac{1}{2\pi\tau C\sqrt{N}}b, \tag{4}$$

where τ is the time the ^{227}AcF beam would take to travel across the interaction region, C is the contrast of the interference fringes, N is the total number of molecules detected across the experimental campaign, and $b = \sqrt{2}$ is a conservative factor that accounts for excess noise in partially closed optical transitions[24], such as the 387-nm transition reported here[27]. For an experiment with a dedicated set-up using ^{227}AcF beams at a kinetic energy of 0.1 keV, an interaction region of 1 m, a fringe contrast of 0.55, the demonstrated ^{227}AcF production rate of 6×10^7 ions per second and a combined efficiency of 2.5% in cooling to the rovibronic ground state, charge exchange, quantum state control and detection, an uncertainty of $\delta f = 1$ mHz would be achieved in 100 days worth of measurements. An uncertainty of $\delta f = 0.1$ mHz could be achieved in the same number of measurement days via a 100-fold

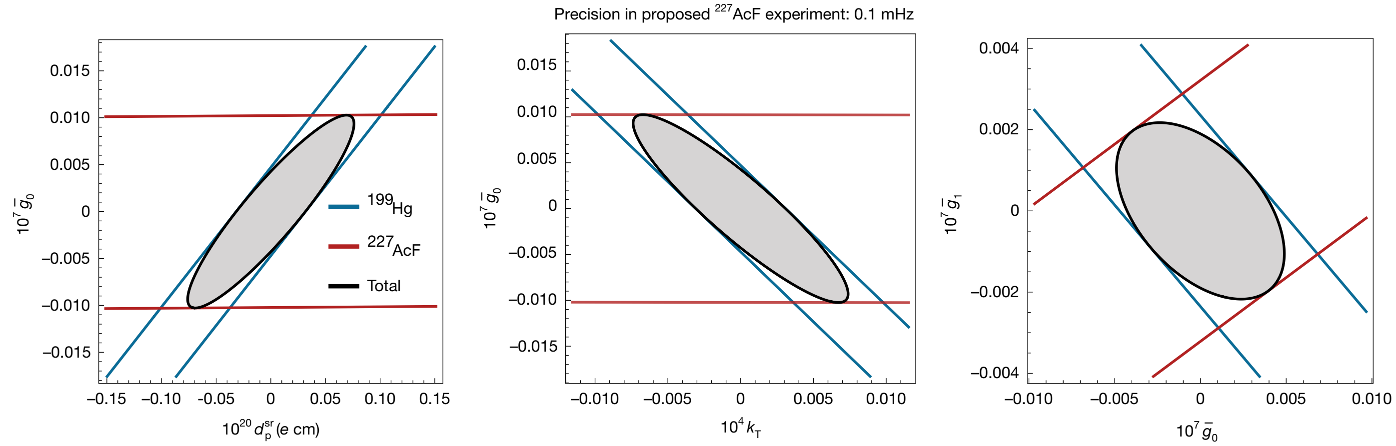

Precision in proposed ^{227}AcF experiment: 0.1 mHz

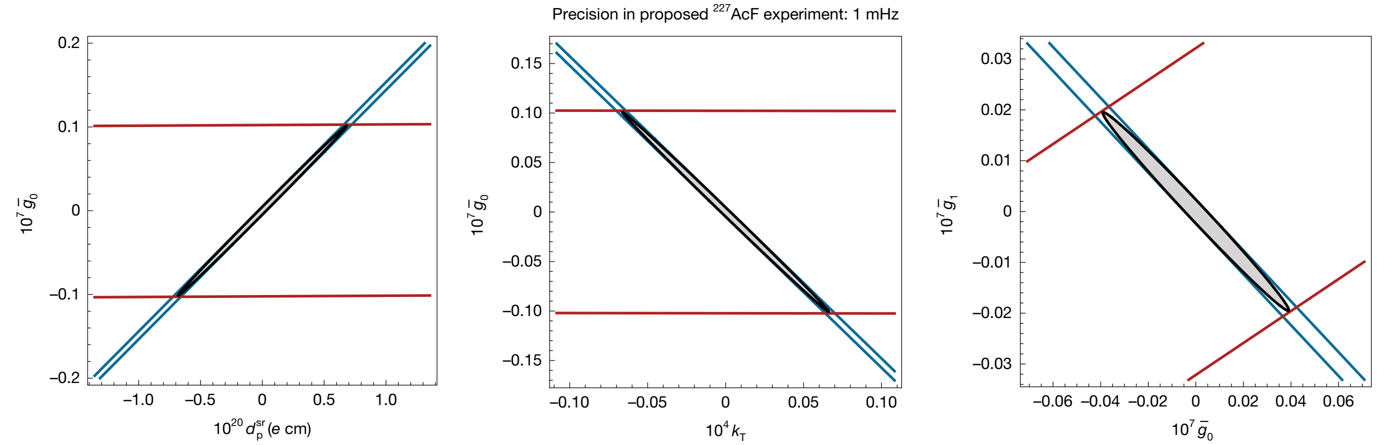

Precision in proposed ^{227}AcF experiment: 1 mHz

Fig. 4 | Cuts of selected two-dimensional subspaces of the full seven-dimensional CP-odd parameter space for different values of experimental precision of a proposed ^{227}AcF experiment. Top: 0.1 mHz. Bottom: 1 mHz. The electronic sensitivity factors for ^{227}AcF used in the analysis, computed at the level of ZORA-cGKS-BHandH, are shown in Extended Data Table 2, the calculated nuclear-structure parameters are given in Table 1, and for the volume interaction with the short-range contribution to the proton EDM we use $R_{\mathrm{vol}} \approx 3.22\ \mathrm{fm}^2$, as discussed in the text. A theoretical uncertainty of 20% is considered, and the molecular sensitivity factors to all CP-odd properties in the hyperspace are conservatively scaled by a factor of 0.8. The impact of a proposed ^{227}AcF experiment is shown in a global analysis including existing experiments using ^{129}Xe (refs. 50,51), ^{171}Yb (ref. 52), ^{133}Cs (ref. 53), ^{199}Hg (ref. 11), ^{205}Tl (ref. 54), ^{225}Ra (refs. 13,55), ^{174}YbF (refs. 48,56), ^{180}HfF$^+$ (ref. 57), ^{205}TlF (ref. 58), ^{207}PbO (ref. 59) and ^{232}ThO (ref. 60), using the experimental data given in the respective references within the global analysis. All electronic-structure parameters for these experiments are taken from ref. 36 and were combined, where available, with nuclear-structure data from ref. 1. In other cases, rough estimates of nuclear-structure parameters from ref. 36 were used. The seven-dimensional ellipsoid is computed at the 95% confidence level. The grey regions mark the two-dimensional slices of the ellipsoid within each two-dimensional subspace.

increase of the production rate, a 100-fold decrease of the kinetic energy, or a combination of such improvements accompanied by improvements in efficiency and fringe contrast. As a molecule homoelectronic to TlF, a similar response to external electric and magnetic fields[12] can be considered for AcF. Therefore, the necessary degree of polarization and the control of stray magnetic fields to limit systematic errors below 1 mHz are achievable with existing technology.

To conclude, the results of this work allow assessment of the potential of ^{227}AcF for searches of CP violation. A spectroscopic study of AcF is demonstrated, revealing an electronic transition at 387 nm, identified to be the strongest transition from the ground state. Rotationally resolved laser spectroscopy of this transition in the future will be a stepping stone for designing dedicated experiments to search for the nuclear Schiff moment of ^{227}Ac.

Owing to the radioactivity of ^{227}Ac, ^{227}AcF beams produced at radioactive ion beam facilities may be envisioned for both further spectroscopy and future precision experiments. Developments are needed for new high-precision experimental techniques using beams directly produced at radioactive ion beam facilities. Gas-jet techniques that have been developed for the study of radioactive atoms, such as in-gas-jet laser ionization spectroscopy[45–47], may be adapted for a precision experiment using ^{227}AcF, as the gas-jet approach was used in the past to set a limit to the electron EDM using ^{174}YbF (ref. 48) and the Schiff moment of ^{205}Tl with ^{205}TlF (ref. 43). The low rotational temperature of molecules produced with this approach would probably be key for improving the signal-to-noise ratio in the spectra compared with this work, and therefore it would also be suited for spectroscopy of excited electronic states. Importantly, further spectroscopic studies on AcF represent essential developments needed to expand current techniques towards also studying other radioactive molecules with complex electronic structure, with impact on fundamental, nuclear and chemical physics[4].

Online content

Any methods, additional references, Nature Portfolio reporting summaries, source data, extended data, supplementary information, acknowledgements, peer review information; details of author contributions and competing interests; and statements of data and code availability are available at https://doi.org/10.1038/s41586-025-09814-1.

1. Chupp, T. E., Fierlinger, P., Ramsey-Musolf, M. J. & Singh, J. T. Electric dipole moments of atoms, molecules, nuclei, and particles. *Rev. Mod. Phys.* **91**, 015001 (2019).
2. Bödeker, D. & Buchmüller, W. Baryogenesis from the weak scale to the grand unification scale. *Rev. Mod. Phys.* **93**, 035004 (2021).

3. Safronova, M. S. et al. Search for new physics with atoms and molecules. *Rev. Mod. Phys.* **90**, 025008 (2018).
4. Arrowsmith-Kron, G. et al. Opportunities for fundamental physics research with radioactive molecules. *Rep. Prog. Phys.* **87**, 084301 (2024).
5. Sakharov, A. Violation of CP invariance, *C* asymmetry, and baryon asymmetry of the Universe. *Sov. Phys. Usp.* **34**, 392 (1991).
6. Schiff, L. I. Measurability of nuclear electric dipole moments. *Phys. Rev.* **132**, 2194–2200 (1963).
7. Flambaum, V. V. & Ginges, J. S. M. Nuclear Schiff moment and time-invariance violation in atoms. *Phys. Rev. A* **65**, 9 (2002).
8. Haxton, W. C. & Henley, E. M. Enhanced *T*-nonconserving nuclear moments. *Phys. Rev. Lett.* **51**, 1937–1940 (1983).
9. Maekawa, C. M., Mereghetti, E., Vries, J. & Kolck, U. The time-reversal- and parity-violating nuclear potential in chiral effective theory. *Nucl. Phys. A* **872**, 117–160 (2011).
10. Dobaczewski, J., Engel, J., Kortelainen, M. & Becker, P. Correlating Schiff moments in the light actinides with octupole moments. *Phys. Rev. Lett.* **121**, 232501 (2018).
11. Graner, B., Chen, Y., Lindahl, E. G. & Heckel, B. R. Reduced limit on the permanent electric dipole moment of ^{199}Hg. *Phys. Rev. Lett.* **116**, 161601 (2016).
12. Grasdijk, O. et al. CeNTREX: a new search for time-reversal symmetry violation in the ^{205}Tl nucleus. *Quantum Sci. Technol.* **6**, 044007 (2021).
13. Bishof, M. et al. Improved limit on the ^{225}Ra electric dipole moment. *Phys. Rev. C* **94**, 1–17 (2016).
14. Flambaum, V. V. & Dzuba, V. A. Electric dipole moments of atoms and molecules produced by enhanced nuclear Schiff moments. *Phys. Rev. A* **101**, 042504 (2020).
15. Scheck, M. et al. A new avenue in the search for CP violation: Mössbauer spectroscopy of ^{227}Ac. *Eur. Phys. J. A* **59**, 116 (2023).
16. Catherall, R. et al. The ISOLDE facility. *J. Phys. G* **44**, 094002 (2017).
17. Au, M. et al. In-source and in-trap formation of molecular ions in the actinide mass range at CERN-ISOLDE. *Nucl. Instrum. Methods Phys. Res. B* **541**, 375–379 (2023).
18. Au, M. *Production of Actinide Atomic and Molecular Ion Beams at CERN-ISOLDE*. PhD thesis, Johannes Gutenberg Univ. Mainz (2023); https://cds.cern.ch/record/2878875?ln=en.
19. Köster, U. et al. (Im-) possible ISOL beams. *Eur. Phys. J. Spec. Top.* **150**, 285–291 (2007).
20. Ballof, J. *Radioactive Molecular Beams at CERN-ISOLDE*. PhD thesis, Johannes Gutenberg Univ. Mainz (2021).
21. Jajčišinová, E. et al. Production study of Fr, Ra and Ac radioactive ion beams at ISOLDE, CERN. *Sci. Rep* .**14**, 11033 (2024).
22. Johnson, J. D. et al. Resonant laser ionization and mass separation of ^{225}Ac. *Sci. Rep.* **13**, 1347 (2023).
23. Au, M. et al. Production and purification of molecular ^{225}Ac at CERN-ISOLDE. *J. Radioanal. Nucl. Chem.* **334**, 367–379 (2024).
24. Lasner, Z. & DeMille, D. Statistical sensitivity of phase measurements via laser-induced fluorescence with optical cycling detection. *Phys. Rev. A* **98**, 53823 (2018).
25. Ho, C. J. et al. New techniques for a measurement of the electron's electric dipole moment. *N. J. Phys.* **22**, 053031 (2020).
26. Athanasakis-Kaklamanakis, M. et al. Electron correlation and relativistic effects in the excited states of radium monofluoride. *Nat. Commun.* **16**, 2139 (2025).
27. Skripnikov, L. V. et al. Ab initio study of electronic states and radiative properties of the AcF molecule. *J. Chem. Phys.* **159**, 124301 (2023).
28. Ramos, J. P. Thick solid targets for the production and online release of radioisotopes: the importance of the material characteristics—a review. *Nucl. Instrum. Methods Phys. Res. B* **463**, 201–210 (2020).
29. Penescu, L., Catherall, R., Lettry, J. & Stora, T. Development of high efficiency Versatile Arc Discharge Ion Source at CERN ISOLDE. *Rev. Sci. Instrum.* **81**, 02–906 (2010).
30. Cocolios, T. E. et al. The Collinear Resonance Ionization Spectroscopy (CRIS) experimental setup at CERN-ISOLDE. *Nucl. Instrum. Methods Phys. Res. B* **317**, 565–569 (2013).
31. Athanasakis-Kaklamanakis, M. et al. Radiative lifetime of the A $^2\Pi_{1/2}$ state in RaF with relevance to laser cooling. *Phys. Rev. A* **110**, 010802 (2024).
32. Skripnikov, L. V., Mosyagin, N. S., Titov, A. V. & Flambaum, V. V. Actinide and lanthanide molecules to search for strong CP-violation. *Phys. Chem. Chem. Phys.* **22**, 18374–18380 (2020).
33. Chen, T. et al. Relativistic exact two-component coupled-cluster study of molecular sensitivity factors for nuclear Schiff moments. *J. Phys. Chem. A* **128**, 6540–6554 (2024).
34. Gaul, K. & Berger, R. Toolbox approach for quasi-relativistic calculation of molecular properties for precision tests of fundamental physics. *J. Chem. Phys.* **152**, 044101 (2020).
35. Chupp, T. & Ramsey-Musolf, M. Electric dipole moments: a global analysis. *Phys. Rev. C* **91**, 035502 (2015).
36. Gaul, K. & Berger, R. Global analysis of $\mathcal{CP}$-violation in atoms, molecules and role of medium-heavy systems. *J. High Energy Phys.* **2024**, 100 (2024).
37. Degenkolb, S., Elmer, N., Modak, T., Mühlleitner, M. & Plehn, T. A global view of the EDM landscape. Preprint at https://arxiv.org/abs/2403.02052 (2024).
38. Dobaczewski, J. & Engel, J. Nuclear time-reversal violation and the Schiff moment of ^{225}Ra. *Phys. Rev. Lett.* **94**, 232502 (2005).
39. Maples, C. Nuclear data sheets for A = 227. *Nucl. Data Sheets* 10.1016/S0090-3752(77)80008-2 (1977).
40. Vries, J., Mereghetti, E. & Walker-Loud, A. Baryon mass splittings and strong CP violation in SU(3) chiral perturbation theory. *Phys. Rev. C* **92**, 45201 (2015).
41. Bsaisou, J. et al. Nuclear electric dipole moments in chiral effective field theory. *J. High Energy Phys.* **2015**, 104 (2015).
42. Yamanaka, N. et al. Probing exotic phenomena at the interface of nuclear and particle physics with the electric dipole moments of diamagnetic atoms: a unique window to hadronic and semi-leptonic CP violation. *Eur. Phys. J. A* **53**, 54 (2017).
43. Cho, D., Sangster, K. & Hinds, E. A. Tenfold improvement of limits on *T* violation in thallium fluoride. *Phys. Rev. Lett.* **63**, 2559–2562 (1989).
44. Ginges, J. S. M. & Flambaum, V. V. Violations of fundamental symmetries in atoms and tests of unification theories of elementary particles. *Phys. Rep.* **397**, 63–154 (2004).
45. Ferrer, R. et al. Towards high-resolution laser ionization spectroscopy of the heaviest elements in supersonic gas jet expansion. *Nat. Commun.* **8**, 14520 (2017).
46. Ferrer, R. et al. Hypersonic nozzle for laser-spectroscopy studies at 17 K characterized by resonance-ionization-spectroscopy-based flow mapping. *Phys. Rev. Res.* **3**, 43041 (2021).
47. Lantis, J. et al. In-gas-jet laser spectroscopy of ^{254}No with JetRIS. *Phys. Rev. Res.* **6**, 23318 (2024).
48. Hudson, J. J. et al. Improved measurement of the shape of the electron. *Nature* **473**, 493–496 (2011).
49. Wolf, R. N. et al. ISOLTRAP's multi-reflection time-of-flight mass separator/spectrometer. *Int. J. Mass Spectrom.* **349–350**, 123–133 (2013).
50. Allmendinger, F. et al. Measurement of the permanent electric dipole moment of the ^{129}Xe atom. *Phys. Rev. A* **100**, 022505 (2019).
51. Sachdeva, N. et al. New limit on the permanent electric dipole moment of ^{129}Xe using ^{3}He comagnetometry and SQUID detection. *Phys. Rev. Lett.* **123**, 143003 (2019).
52. Zheng, T. A. et al. Measurement of the electric dipole moment of ^{171}Yb atoms in an optical dipole trap. *Phys. Rev. Lett.* **129**, 083001 (2022).
53. Murthy, S. A., Krause, D., Li, Z. L. & Hunter, L. R. New limits on the electron electric dipole moment from cesium. *Phys. Rev. Lett.* **63**, 965–968 (1989).
54. Regan, B. C., Commins, E. D., Schmidt, C. J. & DeMille, D. New limit on the electron electric dipole moment. *Phys. Rev. Lett.* **88**, 71805 (2002).
55. Parker, R. H. et al. First measurement of the atomic electric dipole moment of ^{225}Ra. *Phys. Rev. Lett.* **114**, 233002 (2015).
56. Hudson, J. J., Sauer, B. E., Tarbutt, M. R. & Hinds, E. A. Measurement of the electron electric dipole moment using YbF molecules. *Phys. Rev. Lett.* **89**, 23003 (2002).
57. Roussy, T. S. et al. An improved bound on the electron's electric dipole moment. *Science* **381**, 46–50 (2023).
58. Cho, D., Sangster, K. & Hinds, E. A. Search for time-reversal-symmetry violation in thallium fluoride using a jet source. *Phys. Rev. A* **44**, 2783–2799 (1991).
59. Eckel, S., Hamilton, P., Kirilov, E., Smith, H. W. & DeMille, D. Search for the electron electric dipole moment using Ω-doublet levels in PbO. *Phys. Rev. A* **87**, 052130 (2013).
60. Andreev, V. et al. Improved limit on the electric dipole moment of the electron. *Nature* **562**, 355–360 (2018).

Methods

Experiment

Production. The ionization potential of AcF was predicted to lie above the threshold for efficient ionization by contact with a hot surface. In addition, without knowledge of its electronic structure, resonance laser ionization could not be used to produce ion beams of AcF$^+$. The forced-electron-beam-induced arc-discharge (FEBIAD)-type ion source was chosen and operating parameters were identified for the production of AcF$^+$. The UC$_x$ target in the FEBIAD-type ion-source unit was irradiated for 114.4 hours (4.77 days) before the start of the experiment, receiving 1.7×10^{18} protons, or a total of 73.774 µAh. During irradiation, the target unit was kept under vacuum (about 1×10^{-6} mbar) and the target container was resistively heated to slightly above room temperature to prevent condensation during irradiation. At the start of the experiment, the tantalum cathode of the ion source was resistively heated to 1,950 °C to facilitate electron emission. An anode voltage of 100 V was applied to the anode grid to accelerate the electrons and induce ionization within the anode volume, which was also maintained at 100 V with a magnetic-confinement field induced by applying a current of 2.8 A to the ion-source electromagnet. A bias voltage of 40 kV was applied to the target and ion-source unit, such that the ion beam was extracted to the ground potential of the beamline with an energy of 40.1 keV.

The target temperature was increased from about 1,300 °C at the start of the experiment up to 2,000 °C by heating in steps on the order of 10 A to maintain a continuous supply of AcF$^+$. A mix of 10% CF$_4$ and 90% Ar gas was added to the target via a leak of 1.5×10^{-4} mbar l s^{-1} calibrated for He, injecting 0.065 nmol s^{-1} of CF$_4$ for the formation of fluoride molecules.

An extensive beam purity investigation was performed using α-decay spectroscopy of implanted ions and multi-reflection time-of-flight mass spectrometry using the ISOLTRAP apparatus[23,49]. The main expected isobaric contaminant, ^{227}Ra^{19}F$^+$, was eliminated owing to the asynchronous proton irradiation and nuclide extraction, taking advantage of the drastically longer half-life of ^{227}Ac (21.8 years) compared with ^{227}Ra (42 minutes). The time-of-flight spectra in Fig. 1g and Supplementary Fig. 3 show that the ion beam delivered for study was purely composed of ^{227}Ac^{19}F$^+$, with no identifiable contaminants above background.

Collinear resonance ionization spectroscopy. At CRIS, the molecular beam was temporally and spatially overlapped in a collinear geometry with pulsed lasers that step-wise excited the molecular electron to ionization. At the end of the laser–molecule interaction region, the ionized molecules were deflected from the path of the residual neutral beam onto a single-ion detector. The excitation spectra were produced by monitoring the ion count rate on the detector as a function of the laser excitation wavenumbers.

Prior ab initio calculations of the excitation energies in AcF (ref. 27) predicted the (8)$^1\Pi$ state to lie at 26,166(450) cm^{-1} above X$^1\Sigma^+$. The 1σ error of ±450 cm^{-1} required a scanning range of 1,800 cm^{-1} to have 95% probability of discovering the predicted transition. Such a wide range is challenging for continuous scanning of light produced from a single-pass β-barium borate SHG crystal, as the SHG crystal angle requires active stabilization to ensure optimal frequency doubling for all fundamental wavenumbers, while small deviations from the optimal crystal angle also lead to the doubled light exiting the crystal at an angle. The latter issue is exacerbated by the distance between the laser table and the beamline, exceeding 15 m, which means that small exit angles from the SHG crystal lead to the laser light not entering the CRIS beamline.

To compensate for both issues, an active crystal-angle stabilization system was constructed using a ThorLabs PIAK10 piezoelectric inertia actuator, controlled with a proportional-integral-derivative loop reading a fraction of the SHG power output with the help of a beam sampler. To ensure that the second-harmonic light always followed the optimal trajectory for interaction with the molecules in the CRIS interaction region, a commercial active laser-beam stabilization system from MRC Systems was also installed, as shown in Fig. 1. This extended the continuous scanning range from 5 cm^{-1} without stabilization to about 1,450 cm^{-1}.

The observed excitation wavenumber for (8)$^1\Pi \leftarrow$ X$^1\Sigma^+$ was determined by simultaneously monitoring the laser wavenumber and the ion acceleration voltage, defining the kinetic energy of the beam. The wavenumber of the fundamental Ti:Sa laser was monitored with a four-channel HighFinesse WSU-2 wavemeter and the acceleration voltage of the ^{227}AcF$^+$ ions delivered by CERN-ISOLDE was monitored with a 7.5-digit digital multimeter (Keithley DMM7510) with a precision of 100 mV. To trace long-term drifts of the wavemeter, a grating-stabilized diode laser (TOPTICA dlpro) locked to a hyperfine transition in a Rb vapour cell (TEM CoSy) was also continuously monitored by the wavemeter. The small difference in wavelength between the Rb line (about 780 nm) and the fundamental wavelength of the Ti:Sa in this work (about 774 nm) provided confidence that the drift correction is valid in the fundamental wavelength region where the (8)$^1\Pi \leftarrow$ X$^1\Sigma^+$ transition was discovered.

The arc-discharge ion source was chosen to ionize AcF because the molecule's ionization potential (calculated at 6.06(2) eV (ref. 27)) exceeds the work function of rhenium, tantalum and tungsten that are used for high-temperature surface ionization. Ionization by electron bombardment was expected to lead to rotationally hot molecules that may lead to prohibitively low spectroscopic efficiency. To measure the rotational temperature of the beam, the fundamental harmonic of the Ti:Sa laser at 752 nm (in the molecular rest frame) was used in conjunction with the 355-nm non-resonant ionization step to perform spectroscopy of the A$^2\Pi_{1/2} \leftarrow$ X$^2\Sigma_{1/2}$ transition in ^{226}RaF. Using the molecular constants extracted from the rotationally resolved spectroscopy of the molecule[61], the rotational temperature was fitted to extract T_{rot} = 1,200(80) K. In absence of any prior information of the AcF spectra, this temperature was used in the spectroscopic analysis.

Relativistic coupled cluster calculations

The relativistic coupled cluster calculations of the sensitivity W_S of AcF to the nuclear Schiff moment of Ac were carried out using the development version of the DIRAC program[62], which allows the use of relativistic methods within the four-component Dirac–Coulomb Hamiltonian. The single-reference coupled cluster approach with single, double and perturbative triple excitations (CCSD(T)) was used within the finite-field approach, following the implementation presented in ref. 63.

Throughout this study, we used the relativistic Dyall basis sets[64,65] of different quality for the actinium and fluorine atoms; for the W_S calculations, the basis sets for actinium were also manually optimized following the recommendation of ref. 63 and are described in Supplementary Information.

The calculations were carried out at the equilibrium bond distance (R_{e} = 3.974 a_0) obtained via structure optimization carried out at the DC-CCSD(T) level, correlating 50 electrons with active space from −20 E_{h} to 50 E_{h} (corresponding to 4*f*, 5*s*, 5*p*, 5*d*, 6*s*, 6*p*, 7*s* for Ac and 2*s*, 2*p* for F) in units of Hartree energy. The R_{e} optimization was performed using the s-aug-dyall.cv*nz* (n = 2, 3, 4) basis sets and the results were extrapolated to the complete basis set limit (CBSL). For basis set extrapolation, we used the scheme of ref. 66 (H-CBSL).

An extensive computational study was carried out to evaluate the effect of different parameters on the obtained value of the W_S factor and to evaluate the final uncertainty, following procedures used in the past for various atomic and molecular properties[67–71]. The four main sources of uncertainty in these calculations are the incompleteness of the employed basis set, the approximations in the treatment of electron correlation, the missing relativistic effects and the uncertainty in the equilibrium geometry. As we are considering high-order effects, these error sources are assumed to be largely independent, and hence they are treated separately. We consider contributions from the electron–electron Breit interaction and QED effects as the leading missing relativistic contributions. We estimated their order of magnitude by computing the uncorrelated Gaunt term, which can be used to gauge the size of these corrections. Supplementary Information provides details of the computational study and the uncertainty evaluation. Our conservative uncertainty estimate is 7.0%, dominated by the uncertainty in the calculated equilibrium geometry. The final recommended value of W_S is $-7{,}748 \pm 545\, e/4\pi\epsilon_0 a_0^4$.

2c-ZORA-cGHF calculations

On the level of two-component complex generalized Hartree–Fock (cGHF) and two-component complex generalized Kohn–Sham (cGKS) employing the hybrid LDA functional, which includes 50% Fock exchange, proposed by Becke (BHandH)[72], quasirelativistic effects are incorporated within the zeroth-order-regular-approximation (ZORA) framework[73,74]. As suggested by ref. 75, a normalized spherical Gaussian nuclear charge density distribution is used for the isotopes ^{227}Ac and ^{19}F. The gauge dependence of the ZORA framework is alleviated by a model potential as suggested by ref. 76 with additional damping of the atomic Coulomb contribution to the model potential[77].

The wavefunction was obtained self-consistently with convergence achieved when the change in energy between two self-consistent field cycles was less than $10^{-9}\, E_\mathrm{h}$ and the relative change in the spin–orbit-coupling energy contribution was lower than 10^{-13}%. Energy optimizations of the bond lengths were performed up to a change in the Cartesian gradient of $10^{-5}\, E_\mathrm{h}/a_0$. Excited electronic states were obtained self-consistently, using the maximum overlap method (MOM)[78], where the occupation numbers were chosen according to the determinant's overlap with the previous self-consistent field cycle or the initial guess (IMOM[79]). At the Ac centre, Dyall's core-valence triple-ζ basis set with mono-augmentation was used with added s and p functions in an even-tempered manner up to an exponent of 6×10^9 and a multiplicator of 3 (Supplementary Information). At the fluorine centre, Dyall's core-valence triple-ζ basis set was used without additional modifications. All basis sets were employed without contrations.

A characterization of the ground state of AcF and three exemplary excited states, which have not been experimentally observed so far, are shown in Extended Data Table 1.

Utilizing the toolbox approach described in ref. 34, the parity- or time-odd (P,T-odd) properties of the electronic states were obtained as expectation values and from a linear-response ansatz[80,81], respectively, the latter for W_d and W_sps (labelled W_d^m and $W_\mathrm{sps}^\mathrm{m}$). A complete list of the equations for each property is given in Table 6 of ref. 36.

In Extended Data Table 2, P,T-odd properties computed with this method are shown for the states presented in Extended Data Table 1 and compared with the $^3\Delta_1$ states in HfF$^+$, ThO and ThF$^+$, and the $^1\Sigma^+$ states in RaOCH$_3^+$ and TlF.

Vibrational corrections were estimated by solving the vibrational Schrödinger equation within a discrete variable representation on a one-dimensional grid[82] ranging from 3.18 a_0 to 4.77 a_0, divided into 1,000 equidistant points. The properties were interpolated as a sixth-order polynomial function of the bond length, and effects were estimated as described in the supplementary material of ref. 83. The change in the properties as a function of the bond length was computed and is shown in Supplementary Fig. 4a.

The enhancement factor W_S for the nuclear Schiff moment with 2c-ZORA-cGHF evaluates to $W_S = -8{,}400\, e/4\pi\epsilon_0 a_0^4$, whereas further treatment of electron correlation at the level 2c-ZORA-cGKS with the BHandH functional leads to $W_S = -8{,}700\, e/4\pi\epsilon_0 a_0^4$, which is close to the results from CCSD(T). The 2c-ZORA values were obtained after minimization of the energy with respect to the bond length ($R_\mathrm{e} = 4.05 a_0$ compared with CCSD(T) computations $R_\mathrm{e} = 3.97\, a_0$ from this work), suggesting that electron correlation is of importance for the bond length and hence the rotational constant, and, thus, indirectly, also for the sensitivity to CP-odd properties in the ground state of AcF.

When comparing the molecular sensitivity W_S to the nuclear Schiff moment in AcF with that in other closed-shell systems, such as RaOCH$_3^+$ and TlF (Supplementary Fig. 4b), a Z^2 scaling is expected[84], but a reduced enhancement is computed for AcF. Contributions from the individual spinors to W_S show that the bonding spinors—that is, the highest occupied molecular orbital (HOMO)—contribute with sign opposite to the other spinors but with a similar magnitude. In the case of the ground state computed on the level of 2c-cGHF, the HOMO contributes with $29{,}067\, e/4\pi\epsilon_0 a_0^4$ and the remaining orbitals sum up to $-37{,}481\, e/4\pi\epsilon_0 a_0^4$. For excited electronic states, the HOMO contributes to W_S with the same sign but lower magnitude, resulting in a larger value of W_S (see discussion in the main text and Fig. 2b of the supplementary material in ref. 85; also discussion in ref. 33). The suitability of these states for precision experiments depends on their radiative lifetime, among other factors, and thus a discussion is pending experimental observation.

NDFT calculations

The NDFT calculations were performed using the HFODD program[86]. The laboratory Schiff moment, S_lab, can be calculated using second-order perturbation theory as

$$S_\mathrm{lab} \approx \sum_{k \neq 0} \frac{\langle \Psi_0 | \hat{S}_0 | \Psi_k \rangle \langle \Psi_k | \hat{V}_\mathrm{P,T} | \Psi_0 \rangle}{E_0 - E_k} + \text{c.c.}, \tag{5}$$

where $\hat{S}_0$ is the Schiff operator and $\hat{V}_\mathrm{P,T}$ stands for the P,T-violating potential. The index k refers to the excited states with the same angular momentum quantum numbers as the ground state $|\Psi_0\rangle$ but opposite parity. To leading order, the Schiff operator $\hat{S}_0$ is defined as

$$\hat{S}_0 = \frac{e}{10} \sqrt{\frac{4\pi}{3}} \sum_\mathrm{p} \left(r_\mathrm{p}^3 - \frac{5}{3} \overline{r_\mathrm{ch}^2}\, r_\mathrm{p} \right) Y_{10}(\Omega_\mathrm{p}), \tag{6}$$

where the sum ranges over all protons (index p), $Y_{10}(\Omega)$ is the spherical harmonics $Y_{\ell m}(\Omega)$ with ℓ 1, $m = 0$, and $\overline{r_\mathrm{ch}^2}$ is the mean-squared charge radius. In the coordinate representation, $\hat{V}_\mathrm{P,T}$ takes the form[8,9,87]

$$\begin{aligned} &\hat{V}_\mathrm{P,T}(\mathbf{r}_1 - \mathbf{r}_2) \\ &= -\frac{g m_\pi^2}{8\pi m_N} \Big\{ (\boldsymbol{\sigma}_1 - \boldsymbol{\sigma}_2) \cdot (\mathbf{r}_1 - \mathbf{r}_2) \Big[\bar{g}_0 \vec{\tau}_1 \cdot \vec{\tau}_2 - \frac{\bar{g}_1}{2} (\tau_{1z} + \tau_{2z}) + \bar{g}_2 (3\tau_{1z}\tau_{2z} - \vec{\tau}_1 \cdot \vec{\tau}_2) \Big] \\ &\quad - \frac{\bar{g}_1}{2} (\boldsymbol{\sigma}_1 + \boldsymbol{\sigma}_2) \cdot (\mathbf{r}_1 - \mathbf{r}_2)(\tau_{1z} - \tau_{2z}) \Big\} \frac{\exp(-m_\pi |\mathbf{r}_1 - \mathbf{r}_2|)}{m_\pi |\mathbf{r}_1 - \mathbf{r}_2|^2} \left[1 + \frac{1}{m_\pi |\mathbf{r}_1 - \mathbf{r}_2|} \right] \\ &\quad + \frac{1}{2 m_N^3} [\bar{c}_1 + \bar{c}_2 \vec{\tau}_1 \cdot \vec{\tau}_2] (\boldsymbol{\sigma}_1 - \boldsymbol{\sigma}_2) \cdot \nabla \delta^3 (\mathbf{r}_1 - \mathbf{r}_2), \end{aligned} \tag{7}$$

where isovector operators are denoted by arrows, τ_z is +1 (−1) for neutrons (protons), the pion mass is $m_\pi = 0.7045\ \mathrm{fm}^{-1}$, the nucleon mass is $m_N = 4.7565\ \mathrm{fm}^{-1}$, and $\bar{g}_0$, $\bar{g}_1$ and $\bar{g}_2$ are the unknown isoscalar, isovector and isotensor CP-odd pion–nucleon coupling constants, respectively. The strong πNN coupling constant is denoted by g, and $\bar{c}_1$ and $\bar{c}_2$ are the coupling constants of a CP-odd short-range interaction.

The $\mathrm{I}^\pi = \frac{3^-}{2}$ ground state $|\Psi_0\rangle$ of ^{227}Ac has a $\mathrm{I}^\pi = \frac{3^+}{2}$ partner state $|\overline{\Psi}_0\rangle$ at $\Delta E \equiv E_{\overline{\Psi}_0} - E_{\Psi_0} = 27.369$ keV (ref. 39). Owing to the small energy difference ΔE and in the absence of other reported low-lying $\frac{3^+}{2}$ states, equation (5) reduces to

$$S_\mathrm{lab} \approx -2\mathrm{Re} \frac{\langle \Psi_0 | \hat{S}_0 | \overline{\Psi}_0 \rangle \langle \overline{\Psi}_0 | \hat{V}_\mathrm{P,T} | \Psi_0 \rangle}{\Delta E}. \tag{8}$$

In octupole deformed nuclei, the NDFT calculation breaks parity and rotational symmetries, and the obtained nuclear wave function is the deformed quasiparticle vacuum, $|\Phi_0\rangle$, defined in the body-fixed frame of the nucleus. The intrinsic state, $|\Phi_0\rangle$, needs to be projected onto the laboratory states with well-defined angular momentum and parity. In the rigid deformation approximation, the matrix elements in the numerator of equation (8) read:

$$\langle \Psi_0 | \hat{S}_0 \, | \overline{\Psi}_0 \rangle_{\text{rigid}} = \frac{J}{J+1} S_{\text{int}}, \tag{9}$$

$$\langle \overline{\Psi}_0 | \hat{V}_{\text{P,T}} \, | \Psi_0 \rangle_{\text{rigid}} = \langle \hat{V}_{\text{P,T}} \rangle \tag{10}$$

where $J = \frac{3}{2}$ for ^{227}Ac, S_{int} is the intrinsic Schiff moment and $\langle \hat{V}_{\text{P,T}} \rangle$ is the intrinsic expectation value of the operator $\hat{V}_{\text{P,T}}$. In terms of the coupling constants g, $\overline{g}_i$ and $\bar{c}_i$, the expectation value $\langle \hat{V}_{\text{P,T}} \rangle$ can be rewritten as

$$\langle \hat{V}_{\text{P,T}} \rangle = v_0 g\overline{g}_0 + v_1 g\overline{g}_1 + v_2 g\overline{g}_2 + w_1 \bar{c}_1 + w_2 \bar{c}_2. \tag{11}$$

The insertion of equations (9)–(11) into equation (8) leads to the expression of S_{lab} as

$$S_{\text{lab}} = a_0 g\overline{g}_0 + a_1 g\overline{g}_1 + a_2 g\overline{g}_2 + b_1 \bar{c}_1 + b_2 \bar{c}_2, \tag{12}$$

where

$$a_i = -\frac{2J}{J+1} \frac{S_{\text{int}} v_i}{\Delta E} \quad \text{and} \quad b_i = -\frac{2J}{J+1} \frac{S_{\text{int}} w_i}{\Delta E} \tag{13}$$

have units of $e\,\text{fm}^3$.

As shown in ref. 10, there is a strong correlation between the intrinsic Schiff moment S_{int} in one odd nucleus and the intrinsic matrix element of the octupole charge operator[88]

$$\hat{Q}_{30} = e \sum_p r_{\text{p}}^3 Y_{30}(\Omega_{\text{p}}) \tag{14}$$

in another even–even nucleus with close proton and neutron numbers. The correlation is visualized in Supplementary Fig. 5 using several Skyrme functionals within the Hartree–Fock–Bogoliubov method used in this work. For each functional, the neutron and proton pairing strengths were adjusted to reproduce the experimental pairing gaps of ^{229}Th and ^{227}Ac, respectively. The strong correlation between these two observables were used in a scheme to determine the intrinsic Schiff moment of a nucleus without relying on the results obtained with a specific functional. Using a variety of functionals, the intrinsic Schiff moment of ^{227}Ac and the intrinsic electric octupole moment of ^{226}Ra were calculated, and linear regression analysis was performed to determine the relationship between the two correlated observables. The resulting regression line was then used along with the measured value of the electric octupole moment of ^{226}Ra, yielding the value of the intrinsic nuclear Schiff moment of ^{227}Ac reported in this work. Details on the procedure and uncertainty estimation are given in Supplementary Information.

Global analysis

The measurement model of ref. 36 was expanded to explicitly contain two different pion–nucleon coupling constants $\overline{g}_0$, $\overline{g}_1$ and the assumption $d_{\text{p}}^{\text{sr}} = -d_{\text{n}}^{\text{sr}}$, where the suggestions of ref. 37 are followed.

In the Hamiltonian in equation (3), seven fundamental P,T-odd parameters contribute to the total atomic or molecular EDM. Considering experiments using ^{129}Xe (refs. 50,51), ^{171}Yb (ref. 52), ^{133}Cs (ref. 53), ^{199}Hg (ref. 11), ^{205}Tl (ref. 54), ^{225}Ra (refs. 13,55), ^{174}YbF (refs. 48,56), ^{180}HfF$^+$ (ref. 57), ^{205}TlF (ref. 58), ^{207}PbO (ref. 59), ^{232}ThO (ref. 60) and ^{227}AcF, this results in a 12×7 matrix W, where the element in row i and column j corresponds to the Hamiltonian term in equation (3) for atom/molecule i and P,T-odd constant j. Electronic-structure coefficients for all atoms and molecules except AcF were taken from ref. 36 and nuclear-structure coefficients were taken from ref. 1, where available. Otherwise nuclear-structure estimates reported in ref. 36 were used. Combined with the vector of the P,T-odd constants $\mathbf{x}_{\text{PT}}^{\text{T}} = [k_{\text{T}}, k_{\text{p}}, k_{\text{sps}}, \overline{g}_0, \overline{g}_1, d_{\text{e}}, d_{\text{p}}^{\text{sr}}]$ and the vector of the experimental frequency shifts $\mathbf{f}^{\text{T}} = [\delta f_1, \ldots \delta f_7]$, the model is a system of linear equations of the form

$$h\mathbf{f} = \mathbf{W}\mathbf{x}_{\text{PT}}. \tag{15}$$

Following ref. 36, the restrictive power of a set of experiments can be determined by the volume enclosed by an ellipsoid in the seven-dimensional parameter hyperspace for a given confidence level. The global constraints on individual parameters are given by the extrema of the ellipsoid and are provided in Extended Data Table 3. It should be noted that a precision better than 1 mHz in the proposed ^{227}AcF experiment would not further improve global constraints on individual parameters, as these are limited by the experiments with the largest uncertainties (see also ref. 37 for a discussion).

Data availability

The experimental and computational results shown in the figures of this work are included in the source data file available online with this article. Source data for the plots are provided with this paper. Raw measurement data can be provided upon request to the corresponding authors.

Code availability

The code used for the analysis can be provided upon request to the corresponding authors. The codes used to carry out electronic- and nuclear-structure calculations are publicly available and cited in the text; input files can be made available upon request to the corresponding authors. The code used to carry out the global analysis can be made available upon request to the corresponding authors.

61. Udrescu, S. M. et al. Precision spectroscopy and laser-cooling scheme of a radium-containing molecule. *Nat. Phys.* **20**, 202–207 (2024).
62. Bast, R. et al. DIRAC23. *Zenodo* https://doi.org/10.5281/zenodo.7670749 (2023).
63. Gaul, K. et al. $\mathcal{CP}$-violation sensitivity of closed-shell radium-containing polyatomic molecular ions. *Phys. Rev. A* **109**, 042819 (2024).
64. Dyall, K. G. Relativistic double-zeta, triple-zeta, and quadruple-zeta basis sets for the light elements H–Ar. *Theor. Chem. Acc.* **135**, 128 (2016).
65. Dyall, K. G. Relativistic double-zeta, triple-zeta, and quadruple-zeta basis sets for the 4*s*, 5*s*, 6*s*, and 7*s* elements. *J. Phys. Chem. A* **113**, 12638–12644 (2009).
66. Helgaker, T., Klopper, W., Koch, H. & Noga, J. Basis-set convergence of correlated calculations on water. *J. Chem. Phys.* **106**, 9639–9646 (1997).
67. Hao, Y. et al. Nuclear anapole moment interaction in BaF from relativistic coupled-cluster theory. *Phys. Rev. A* **98**, 032510 (2018).
68. Guo, Y., Pašteka, L. F., Eliav, E. & Borschevsky, A. Ionization potentials and electron affinity of oganesson with relativistic coupled cluster method. *Adv. Quantum Chem.* **83**, 107–123 (2021).
69. Haase, P. A. B., Eliav, E., Iliaš, M. & Borschevsky, A. Hyperfine structure constants on the relativistic coupled cluster level with associated uncertainties. *J. Phys. Chem. A* **124**, 3157–3169 (2020).
70. Leimbach, D. et al. The electron affinity of astatine. *Nat. Commun.* **11**, 3824 (2020).
71. Kyuberis, A. A. et al. Theoretical determination of the ionization potentials of CaF, SrF, and BaF. *Phys. Rev. A* **109**, 022813 (2024).
72. Becke, A. D. A new mixing of Hartree–Fock and local density-functional theories. *J. Chem. Phys.* **98**, 1372–1377 (1993).
73. Chang, C., Pelissier, M. & Durand, P. Regular two-component Pauli-like effective Hamiltonians in Dirac theory. *Phys. Scr.* **34**, 394–404 (1986).
74. Lenthe, E., Baerends, E.-J. & Snijders, J. G. Relativistic regular two-component Hamiltonians. *J. Chem. Phys.* **99**, 4597 (1993).
75. Visscher, L. & Dyall, K. G. Dirac–Fock atomic electronic structure calculations using different nuclear charge distributions. *At. Data Nucl. Data Tables* **67**, 207–224 (1997).
76. Wüllen, C. Molecular density functional calculations in the regular relativistic approximation: method, application to coinage metal diatomics, hydrides, fluorides and chlorides, and comparison with first-order relativistic calculations. *J. Chem. Phys.* **109**, 392–399 (1998).
77. Liu, W., Wüllen, C., Wang, F. & Li, L. Spectroscopic constants of MH and M_2 (M = Tl, E113, Bi, E115): direct comparisons of four- and two-component approaches in the framework of relativistic density functional theory. *J. Chem. Phys.* **116**, 3626–3634 (2002).
78. Gilbert, A. T. B., Besley, N. A. & Gill, P. M. W. Self-consistent field calculations of excited states using the maximum overlap method (MOM). *J. Phys. Chem. A* **112**, 13164–13171 (2008).

79. Barca, G. M. J., Gilbert, A. T. B. & Gill, P. M. W. Simple models for difficult electronic excitations. *J. Chem. Theory Comput.* **14**, 1501–1509 (2018).
80. Brück, S. A., Sahu, N., Gaul, K. & Berger, R. Quasi-relativistic approach to analytical gradients of parity violating potentials. *J. Chem. Phys.* **158**, 194109 (2023).
81. Colombo Jofré, M. T. et al. Relativistic and QED corrections to one-bond indirect nuclear spin-spin couplings in X_2^{2+} and X_2^{2+} ions (X = Zn, Cd, Hg). *J. Chem. Phys.* **157**, 064103 (2022).
82. Meyer, R. Trigonometric interpolation method for one-dimensional quantum-mechanical problems. *J. Chem. Phys.* **52**, 2053–2059 (1970).
83. Udrescu, S. M. et al. Isotope shifts of radium monofluoride molecules. *Phys. Rev. Lett.* **127**, 033001 (2021).
84. Sushkov, O. P., Flambaum, V. V. & Khriplovich, I. B. Possibility of investigating P- and T-odd nuclear forces in atomic and molecular experiments. *Zh. Eksp. Teor. Fiz* **87**, 1521 (1984).
85. Zülch, C., Gaul, K., Giesen, S. M., Ruiz, R. F. G. & Berger, R. Cool molecular highly charged ions for precision tests of fundamental physics. Preprint at https://arxiv.org/abs/2203.10333 (2022).
86. Dobaczewski, J. et al. Solution of universal nonrelativistic nuclear DFT equations in the Cartesian deformed harmonic-oscillator basis. (IX) HFODD (v3.06h): a new version of the program. *J. Phys. G* **48**, 102001 (2021).
87. Herczeg, P. *T*-violation in nuclear interactions—an overview. *Hyperfine Interact.* **43**, 75–93 (1988).
88. Ring, P. & Schuck, P. *The Nuclear Many-Body Problem* 1st edn (Springer, 1980).

Acknowledgements Authors L.S. and N.S.M. are affiliated with an institute formerly covered by a cooperation agreement with CERN. We thank A. Zaitsevskii and A. Oleynichenko for help with electronic-structure calculations; and V. V. Flambaum, E. Wursten and C. J. Ho for discussions. The research leading to these results has received funding from the European Union's Horizon Europe research and innovation programme under grant agreement number 101057511. Financial support from FWO, as well as from the Excellence of Science (EOS) programme (number 40007501) and the KU Leuven project C14/22/104, is acknowledged. The STFC consolidated grants ST/V001116/1 and ST/P004423/1 and the FNPMLS ERC grant agreement 648381 are acknowledged. Swedish Research Council (grant number 2020-03505) and funding from the European Union's Horizon 2020 research and innovation programme under the Marie Skłodowska-Curie Grant Agreement number 861198 are acknowledged. This work was partially supported by the STFC Grant numbers ST/P003885/1 and ST/V001035/1, and by a Leverhulme Trust Research Project Grant. K.G. thanks the Fonds der Chemischen Industrie (FCI) for generous funding through a Liebig fellowship. This project was partly undertaken on the Viking Cluster, which is a high-performance compute facility provided by the University of York. We are grateful for computational support from the University of York High Performance Computing service, Viking and the Research Computing team. C.Z. and R.B. acknowledge financial support by the Deutsche Forschungsgemeinschaft (DFG, German Research Foundation) with the project number 445296313. C.Z., K.G. and R.B. acknowledge computing time provided at the NHR Center NHR@SW at Goethe-University Frankfurt. This was funded by the Federal Ministry of Education and Research and the state governments participating on the basis of the resolutions of the GWK for national high-performance computing at universities (http://www.nhr-verein.de/unsere-partner). A.B. and A.K. thank the Center for Information Technology at the University of Groningen for their support and for providing access to the Peregrine and Hábrók high-performance computing clusters. A.B. is grateful for the Dutch Research Council (NWO) project number Vi.Vidi.192.088. R.F.G.R., S.G.W., and F.P. acknowledge funding from the Office of Nuclear Physics, US Department of Energy, under grants DE-SC0021176 and DE-SC0021179.

Author contributions M.A.-K., M.A., A.K., C.Z., K.G., H.W. and G.N. led the paper preparation. M.A.-K., M.A., A.K., C.Z., K.G., L.L., J.R.R., Á.K., S.B., J.B., R.B., C.B., A.A.B., K.C., T.E.C., R.P.d.G., A.D., K.T.F., S.F., J.D.J., R.F.G.R., D.H., S.K., Y.C.L., K.M.L., A.M., G.N., M.N., L.N., F.P., S.R., B.v.d.B., J.W., S.G.W. and X.F.Y. performed the experiment. A.K. and A.B. performed the relativistic coupled cluster calculations and reviewed the results. C.Z., K.G. and R.B. performed the 2c-ZORA-cGHF calculations and the global analysis and reviewed the results. L.S. performed the electronic-structure calculations of molecular terms and Franck–Condon factors and reviewed the results., and N.S.M. constructed the pseudopotentials for these electronic-structure calculations and reviewed the results. H.W. and J.D. performed the nuclear DFT calculations, and H.W., J.D. and W.R. reviewed the results. M.A.-K. and A.A.B. performed the data analysis. All co-authors participated in editing and revising the paper.

Competing interests The authors declare no competing interests.

Additional information
Supplementary information The online version contains supplementary material available at https://doi.org/10.1038/s41586-025-09814-1.
Correspondence and requests for materials should be addressed to M. Athanasakis-Kaklamanakis, M. Au or G. Neyens.
Peer review information *Nature* thanks the anonymous reviewers for their contribution to the peer review of this work. Peer reviewer reports are available.
Reprints and permissions information is available at http://www.nature.com/reprints.

Extended Data Table 1 | Qualitative characterization at the level of 2c-ZORA-cGHF for the electronic ground state and some excited electronic states in AcF

State	Term symbol	$\langle\Omega\rangle$	$\langle\Lambda\rangle$	R_e / a_0	$\tilde{\omega}_\mathrm{e}$ / cm^{-1}	$\Delta\tilde{\nu}_\mathrm{T}$ / cm^{-1}	M_1/%	M_2/%
X	$^1\Sigma^+$	0.00	0.00	4.05	528	0	89s,5p,6d	89s,5p,6d
X (BHandH)	$^1\Sigma^+$	0.00	0.00	3.98	—	—	89s,4p,7d	89s,4p,7d
Excited state 1	$^3\Delta_1$	1.00	2.00	4.11	501	4760	87s,7p,6d	100d
Excited state 2	$^3\Phi_2$	2.00	2.93	4.13	483	17 100	99d	55p,42d
Excited state 3	$^1\Sigma^+$	0.00	0.00	4.14	480	23 600	98d	98d

Shown are the expectation values for the projection of the total electron angular momentum <Ω> and electron orbital angular momentum <Λ> along the molecular axis, the equilibrium bond lengths R_e, the harmonic vibrational wavenumber $\tilde{\omega}_e$, the transition wavenumber $\Delta\tilde{\nu}_T$ from the electronic ground state, and the spinor contributions M_i on the Ac center from an atomic picture for the two highest occupied spinors (i = 1, 2) obtained via a Mulliken analysis.

Extended Data Table 2 | *P,T*-odd properties obtained on the level of 2c-cGHF and 2c-cGKS/BHandH

	State	$\langle\Omega\rangle$	$W_\mathcal{S}/\frac{e}{4\pi\epsilon_0 {a_0}^4}$	$W_\mathrm{d}/\frac{\mathrm{GV}}{\mathrm{cm}}$	$W_\mathrm{sps}/\mathrm{peV}$	$W_\mathrm{T}/\mathrm{peV}$	$W_\mathrm{p}/\mathrm{feV}$	$W_\mathrm{m}/\frac{\mathrm{kV}\eta_\mathrm{p}}{\mathrm{cm}\mu_\mathrm{N}}$
HfF^+ [82]	${}^3\Delta_1$	1.00	−15 000	26.5	95.1	−4.55	−17.0	309
ThO [82]	${}^3\Delta_1$	1.00	−35 000	99.9	584	−14.6	−57.5	166
ThF^+ [36]	${}^3\Delta_1$	1.00	−45 600	43.5	248	−17.4	−69.1	603
$RaOCH_3^+$ (4c-DHF) [63]	${}^1\Sigma^+$	0.00	−56 300	−0.0112	−0.298	−20.7	−81.5	959
TlF [36]	${}^1\Sigma^+$	0.00	45 850	0.008 00	0.247	19.4	72.2	−777
AcF: *X*	${}^1\Sigma^+$	0.00	−8400	−0.000 450	−0.0215	−1.63	−6.73	38.8
AcF: *X* (BHandH)	${}^1\Sigma^+$	0.00	−8700	−0.001 20	−0.0293	−1.94	−7.90	33.0
AcF: Excited state 1	${}^3\Delta_1$	1.00	−28 000	−64.2	−365	−9.76	−38.7	395
AcF: Excited state 2	${}^3\Phi_2$	2.00	−49 000	−19.7	−132	−20.4	−80.3	842
AcF: Excited state 3	${}^1\Sigma^+$	0.00	−53 000	—	—	−19.3	−76.4	874

The properties are computed on the energy-optimized structure of the respective methods and electronic states. For closed-shell systems with term symbol ${}^1\Sigma^+$, the magnetic contributions to W_d and W_sps are given. The computation for $RaOCH_3^+$ from ref. 63 was done at the level of 4c Dirac–Hartree–Fock (4c-DHF). HfF^+ and ThO data are from R. Simpson et al., unpublished data.

Extended Data Table 3 | Comparison of global bounds on sources of *P,T*-violation with and without the proposed ^{227}AcF experiment with an experimental uncertainty of 1 mHz

Source	Global limit without ^{227}AcF	Global limit with ^{227}AcF
$d_\mathrm{e}/(e\,\mathrm{cm})$	4×10^{-29}	4×10^{-29}
$d_\mathrm{p}^\mathrm{sr}/(e\,\mathrm{cm})$	4×10^{-22}	2×10^{-23}
k_sps	1×10^{-8}	1×10^{-8}
k_T	8×10^{-6}	4×10^{-6}
k_p	3×10^{-3}	9×10^{-4}
$\bar{g}_0$	6×10^{-9}	6×10^{-10}
$\bar{g}_1$	4×10^{-9}	2×10^{-10}

Global bounds are obtained from seven-dimensional ellipsoidal coverage regions at 95% confidence level, including existing experiments with ^{129}Xe[50,51], ^{171}Yb[52], ^{133}Cs[53], ^{199}Hg[11], ^{205}Tl[54], ^{225}Ra[13,55], ^{174}YbF[48,56], ^{180}HfF^{+}[57], ^{205}TlF[58], ^{207}PbO[59], and ^{232}ThO[60]. All electronic-structure parameters for these experiments were taken from ref. 36 and were combined, where available, with nuclear-structure data from ref. 1. In other cases, estimates of nuclear-structure parameters from ref. 36 were employed. A conservative theoretical uncertainty of 20% is assumed and the electronic-structure sensitivity factors to all sources are scaled by a factor of 0.8 to account for a worst-case scenario.